Research Square

Preprints are preliminary reports that have not undergone peer review.
They should not be considered conclusive, used to inform clinical practice,
or referenced by the media as validated information.

Study on blast resistance prediction model for a CFRP–steel plate composite structure based on deep learning

Xiaowang Sun

xwsun@njust.edu.cn

Nanjing University of Science and Technology

Hao Sun

Nanjing University of Science and Technology

Jiahao He

Nanjing University of Science and Technology

Hejing Hou

Nanjing University of Science and Technology

Haopeng Bao

Nanjing University of Science and Technology

Xianhui Wang

Nanjing University of Science and Technology

Tao Wang

Nanjing University of Science and Technology

Tiaoqi Fu

Nanjing University of Science and Technology

Sha Chen

Chongqing Changan Industry (Group) Co., Ltd.

Tingjun Liu

Chongqing Changan Industry (Group) Co., Ltd.

Research Article

Keywords: CFRP, Prediction model, Deep learning algorithm, Blast resistance

Posted Date: November 26th, 2026

DOI: https://doi.org/10.21203/rs.3.rs-11818952/v1

License: This work is licensed under a Creative Commons Attribution 4.0 International License.
Read Full License

Additional Declarations: No competing interests reported.

Study on blast resistance prediction model for a CFRP–steel plate composite structure based on deep learning

Xiaowang Sun[1], Hao Sun[1], Jiahao He[1], Hejing Hou[1], Haopeng Bao[1], Xianhui Wang[1], Tao Wang[1], Tiaoqi Fu[1], Sha Chen[2], Tingjun Liu[2].

1 *Nanjing University of Science and Technology*

2 *Chongqing Changan Industry (Group) Co., Ltd.*

Abstract: Carbon fiber-reinforced polymer (CFRP), which is characterized by its high strength-to-weight ratio and lightweight nature, has demonstrated significant potential for structural protection against blast loads. In this study, an improved elephant herding optimization–general regression neural network (IEHO-GRNN) algorithm was developed to construct a prediction model correlating the CFRP material parameters with structural blast resistance, and its predictive accuracy was systematically evaluated. Initially, near-field air blast tests on CFRP-strengthened steel-plate composite structures were conducted to validate the reliability of the numerical simulation model. Subsequently, based on an orthogonal experimental design and the random forest algorithm, the key parameters influencing the blast performance were identified. Uniform sampling within the parameter space was then performed to establish training and test datasets. The predictive capabilities of five deep learning algorithms—the back propagation neural network, radial basis function neural network, general regression neural network (GRNN), elephant herding optimization–GRNN algorithms, and the proposed IEHO-GRNN algorithm—were comprehensively assessed using five error metrics. The results indicated that the in-plane shear modulus, out-of-plane Poisson's ratio, tensile strengths in the warp and weft directions, and out-of-plane compressive strength were the critical material parameters governing the blast resistance of CFRP–steel composite structures. Furthermore, the mapping model constructed using the IEHO-GRNN algorithm achieved a superior prediction accuracy, with a coefficient of determination R^2 exceeding 0.95.

Keywords: CFRP; Prediction model; Deep learning algorithm; Blast resistance

1 Introduction

In recent years, the escalation of regional terrorism and frequent local conflicts have posed severe threats to regional stability, as well as civilian lives and property, primarily due to accidents induced by explosions [1,2]. Previous studies have indicated that merely increasing the steel substrate thickness to enhance the protective performance significantly elevates the overall structural mass, thereby compromising the mobility and passability of the equipment. In contrast, carbon-fiber reinforced polymer (CFRP) offers distinct advantages—it is lightweight and has high specific strength and stiffness—making it effective in mitigating blast shock waves. However, its poor penetration resistance limits its application as a standalone protective structure [3]. Kim et al. [4] proposed a hybrid anti-blast system composed of steel plates and CFRP, verifying its capacity to withstand uncertain blast loads via reliability-based methods. Sayam et al. [5] systematically reviewed the mechanical properties and structural applications of CFRP, highlighting that the fiber-related material parameters significantly influence the structural mechanical performance. Consequently, establishing a clear mapping relationship between the CFRP material parameters and the structural protective performance is essential not only for accurately predicting the blast resistance but also for providing theoretical support for the optimized design of protective structures.

To address the challenges of high experimental costs and intensive computational resource requirements associated with finite element simulations, researchers have proposed surrogate modeling techniques to map the CFRP material parameters to the structural performance. Surrogate models,

grounded in data-driven approaches and integrating mathematical statistics with machine learning, approximate complex functional relationships for prediction purposes [6]. Traditional surrogate models, relying on statistical theories and machine learning, have yielded numerous achievements. For instance, Zhang et al. [7] developed mapping relationships between the parameters (e.g., the single-layer thickness, density, and ply angles) and the static strength of aircraft CFRP elevators using Kriging, polynomial chaos Kriging, and support vector regression, validating their predictive accuracy. Similarly, Alsheghri et al. [8] constructed multiple surrogate models based on ridge regression, random forest regression, and support vector regression to predict the flexural strength of CFRP, incorporating variables such as the glass transition temperature and volume fractions. Their results confirmed the reliability and applicability of these models. However, traditional surrogate models often rely on manual intervention for feature extraction and have subjective feature selection and weak generalization capabilities. In contrast, deep learning algorithms can automatically extract high-order features from raw data, rendering them suitable for modeling multidimensional, massive, and nonlinear problems.

With the maturation of deep learning technologies, neural network algorithms such as the backpropagation neural network (BPNN), radial basis function neural network (RBF), and general regression neural network (GRNN) have been widely adopted in composite material performance prediction. Cao et al. [9] employed a BPNN to predict the ballistic performance of glass-fiber composites, demonstrating that the method reduced the workload through autonomous learning rules; however, it was prone to local optima, leading to suboptimal accuracy. Li et al. [10] constructed a performance prediction model for starch-based foamed composites based on RBF theory, noting an improved training efficiency by avoiding complex iterations; yet, its performance on unseen data remained limited. Saravanakumar et al. [11] utilized a GRNN to predict the wear rate of AA2219–graphite composites, reporting a high prediction efficiency without iterative parameter tuning; nevertheless, the GRNN exhibited extreme sensitivity to the smoothing factor, potentially compromising accuracy.

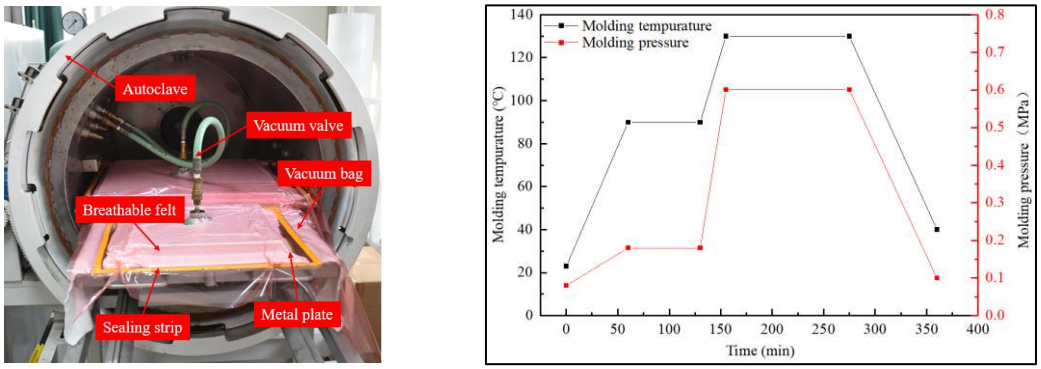
In summary, there is currently a lack of literature establishing a surrogate model for the prediction of blast resistance in CFRP–steel systems, and existing models have inherent shortcomings in terms of prediction robustness. Therefore, an improved elephant herding optimization–general regression neural network (IEHO-GRNN) algorithm is proposed in this paper to construct a prediction model that correlates the material parameters with the blast resistance. First, a blast simulation model for CFRP-strengthened steel composite structures was established and validated against near-field air blast experiments to ensure numerical reliability. Subsequently, combined with finite element simulation results and the random forest algorithm, the key material parameters affecting the blast performance were screened. Based on these parameters, an optimal Latin hypercube sampling (OLHS) method was employed to generate a dataset. Furthermore, five deep learning methods (BPNN, RBF, GRNN, elephant herding optimization–GRNN (EHO-GRNN), and IEHO-GRNN) were utilized to establish prediction models, which were systematically evaluated using five error metrics. Finally, the generalization capability of the optimal model was verified to assess its applicability and stability in practical engineering applications.

2 Blast test

2.1 Specimen preparation

The 12K-T800 grade plain-weave CFRP prepreg (model SYT55) used in this test was produced by Zhongfu Shenying Company. The CFRP prepreg consisted of 0°/90° orthogonally woven fiber

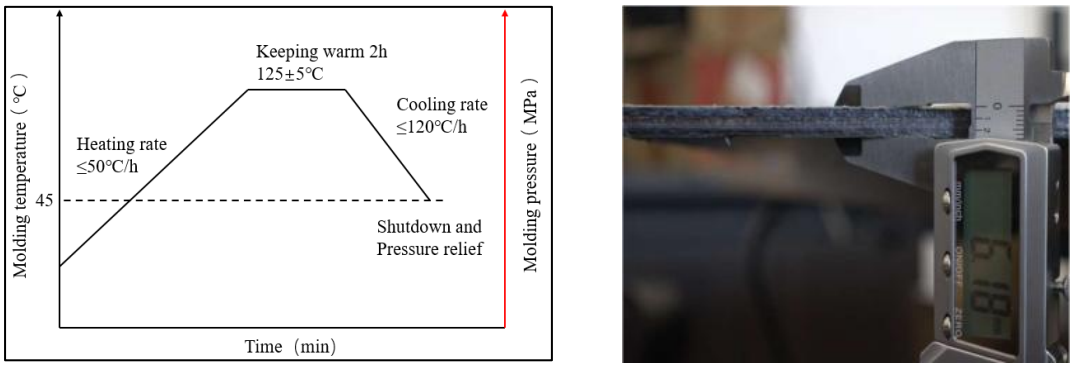
bundles and medium-temperature cured epoxy resin, with a fiber volume fraction of approximately 58% and a nominal thickness of 0.45 mm per layer. When preparing the CFRP, the cut prepreg was laid up in the order of $[0/90]_9$ (9 indicates the number of plies), followed by pre-pressing and encapsulation. It was then evacuated to a vacuum state using an air pump and sent into an autoclave, as shown in Fig. 1(a). The three preparation processes, i.e., heating and pressurizing, maintaining temperature and pressure, and cooling and depressurizing, were completed according to the curing curve provided by the manufacturer, as shown in Fig. 1(b).



(a) Autoclave curing process (b) Autoclave curing curve

Figure. 1. Autoclave curing process

After the preparation of the CFRP laminated board, a plain-woven CFRP–steel plate composite structure was prepared. The total thickness of the CFRP in the composite structure was approximately 4 mm, and the total thickness of the steel plate was approximately 2 mm. Xu et al. [12] studied the explosion-resistant performance of different configurations of CFRP–steel plate composite structures and found that the S+C configuration (steel plate on the front, CFRP on the back) exhibited the best explosion-resistant performance enhancement effect. In this study, the plain-woven CFRP–steel plate composite structure was prepared by laying CFRP on the back of a steel plate. First, a CNC cutting machine was used to cut the steel plate into a 500 mm × 500 mm square. Then, a grinding machine was used to polish the surface of the Q235 steel plate to enhance the bonding strength between it and the laminated board. Next, an ISF-130A-F adhesive film was applied to both the steel plate and the laminated board surfaces to be bonded. Then, the adhesive film was secondarily cured according to the autoclave process parameters shown in Fig. 2(a). The finally prepared plain-woven CFRP–steel plate composite structure is shown in Fig. 2(b).



(a) Secondary curing curve of autoclave (b) Test specimen

Figure. 2. Secondary curing curve and test specimen

2.2 Experimental testing and results

Fig. 3 shows the specific setup for this explosion test. The test rig had external dimensions of 1200 mm × 1200 mm × 460 mm, enclosed and welded with 15-mm-thick steel plates on all sides, and

reinforced with 20 additional 4-mm rectangular tubes. The target plate was positioned between a 1200 mm × 1200 mm × 25 mm base plate of the rig and a 700 mm × 700 mm × 15 mm cover plate, with the three components fixedly connected through 24 M20 bolts. The cylindrical TNT charge with a mass of 200 g, a diameter of 54 mm, and a height of 54 mm was used in the blast test. The clear distance between the bottom surface of the charge and the upper surface of the target plate was 100 mm. Accordingly, the stand-off distance measured from the charge centroid to the target surface was 127 mm.

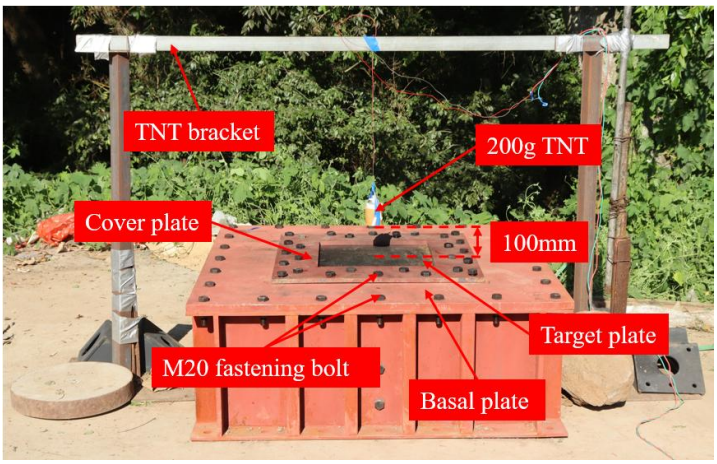
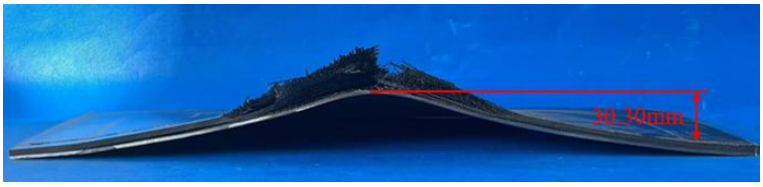
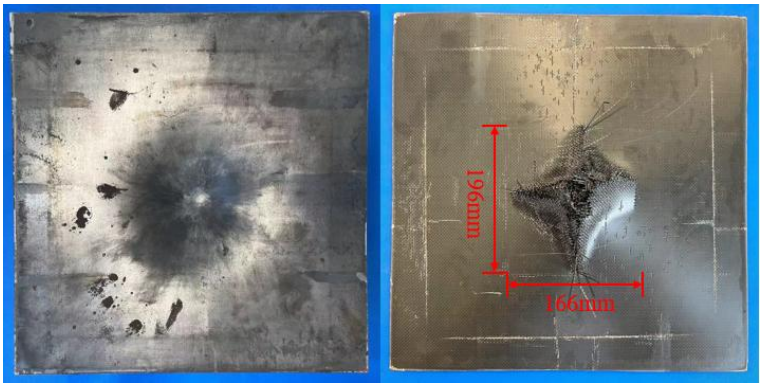


Figure. 3. Test device setup

The damage condition of the plain-woven CFRP–steel plate composite structure after the test is shown in Fig. 4. The cross-sectional damage condition of the composite structure is shown in Fig. 4(a), from which it can be observed that delamination damage occurred in the central area of the composite structure, and there was a slight debonding phenomenon between the carbon-fiber laminate and the steel plate. The plastic displacement of the steel plate measured by a three-dimensional scanner was 30.30 mm. The front and back damage conditions of the composite structure are shown in Fig. 4(b), from which it can be observed that the central area of the steel plate exhibited an indentation phenomenon, while the central area of the carbon-fiber laminate experienced tensile fracture damage, and the breakage was in a cross shape. The measured lengths of the breakage in the horizontal and vertical directions were 166 and 196 mm, respectively.



(a) Cross-sectional damage



(b) Front and back damage

Figure. 4. Experimental damage results of plain weave CFRP–steel plate composite structure

3 Numerical simulation

3.1 Finite element modeling

Due to the symmetry of the test setup, the 1/4 finite element model shown in Fig. 5 was established to enhance the computational efficiency. The one-quarter finite-element model consisted of one quarter of the CFRP laminate, Q235 steel plate, cohesive interfaces, cover plate, and base plate. The explosive and surrounding air were not explicitly meshed. Instead, a 200 g TNT-equivalent air-blast source was prescribed using the CONWEP incident-wave formulation in Abaqus/Explicit. Since the dimensions of the base plate and cover plate had no impact on the simulation results, their outer lengths and widths were set to 300 mm, with thicknesses of 25 and 15 mm, respectively. A grid cell size of 10 mm was employed for discretization. The composite structure consisted of CFRP, steel plates, and zero-thickness cohesive elements, with lengths and widths of 250 mm. The grid cell sizes for the CFRP and steel plates along the thickness direction were 0.4 and 1 mm, respectively. A refined grid of 2 mm was used in a densified area of 100 mm × 100 mm at the center of the target plate, while the peripheral area transitioned to a grid cell size of 6 mm following a gradual change principle, balancing computational accuracy and efficiency. To simulate the constraints imposed on the composite structure and its contact interaction with the explosive shock wave, fixed constraints were applied to the edges of the base and cover plates, symmetric constraints were imposed on the symmetric sections of the model, and general contacts were set globally.

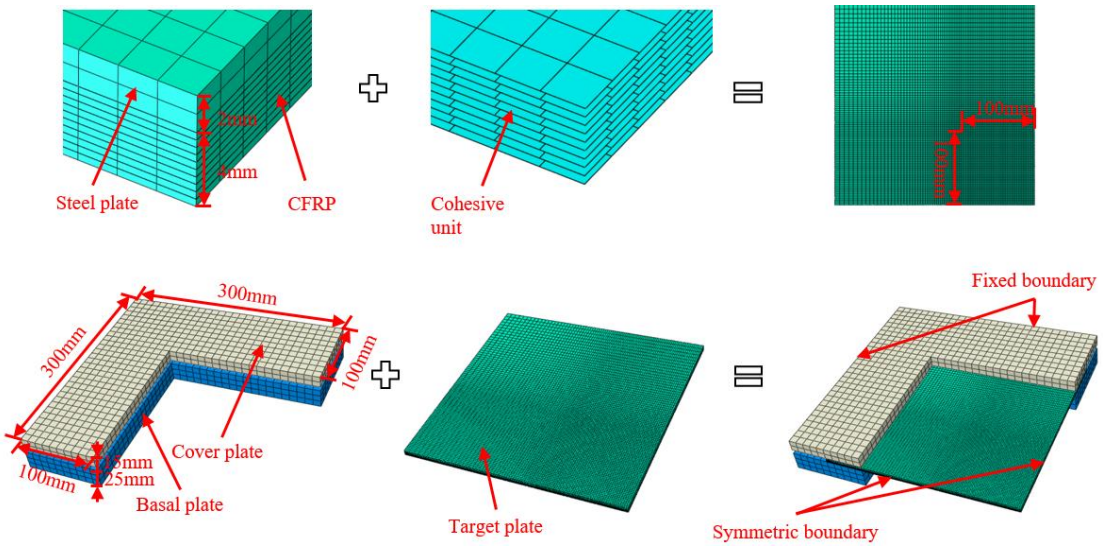


Figure. 5. One-quarter finite element model of plain-weave CFRP-steel composite plate considering symmetric boundary conditions for blast simulation

3.2 Material parameters

The initiation of damage in the plain-weave CFRP was assessed using a modified three-dimensional Hashin failure criterion [13,14], which categorizes carbon-fiber damage into six modes, each corresponding to distinct stress–strain conditions and failure criteria:

Tensile failure in warp direction (ε_{11}>0):

$$R_{1T} = \left(\frac{\sigma_{11}}{X_{1T}}\right)^2 + \left(\frac{\sigma_{13}}{S_{13}}\right)^2, \tag{1}$$

Compression failure in warp direction (ε_{11}<0):

$$R_{1C} = \left(\frac{\sigma_{11}}{X_{1C}}\right)^2, \tag{2}$$

Tensile failure in the weft direction (ε_{22}>0):

$$R_{2T} = \left(\frac{\sigma_{22}}{Y_{2T}}\right)^2 + \left(\frac{\sigma_{23}}{S_{23}}\right)^2, \tag{3}$$

Compression failure in the weft direction (ε_{22}<0):

$$R_{2C} = \left(\frac{\sigma_{22}}{Y_{2C}}\right)^2, \tag{4}$$

Out-of-plane compression failure (ε_{33}<0):

$$R_{3C} = \left(\frac{\sigma_{33}}{Z_{3C}}\right)^2, \tag{5}$$

In-plane shear failure (ε_{12}<0):

$$R_{12} = \left(\frac{\sigma_{12}}{S_{12}}\right)^2, \tag{6}$$

where X_{1T} and X_{1C} represent the tensile and compressive strengths in the warp direction, respectively, Y_{2T} and Y_{2C} represent the tensile and compressive strengths in the weft direction, respectively, Z_{3C} represents the out-of-plane compressive strength, S_{13} and S_{23} represent the out-of-plane shear strengths, and S_{12} represents the in-plane shear strength. When $R_i \leq 1$, the material is in an elastic state; when $R_i \geq 1$, the material is in a failure state. To simulate the gradual degradation of the mechanical properties during material failure, a continuous progressive damage model was adopted. The damage evolution function of this model is

$$\omega_i = 1 - \exp\left(\frac{1}{m_i e}(1 - R_i)^{m_i}\right), \tag{7}$$

where $i = [1T, 1C, 2T, 2C, 3C, 12]^T$, m_i denotes the softening coefficient of the material under each failure mode, and e represents the Napier constant. The exponential growth of this damage evolution function is controlled by m, with a larger m indicating a faster damage evolution of the material.

When damage occurs to a material, its stiffness will also degrade, and the stress–strain relationship after degradation is as follows:

$$\varepsilon = S_d \sigma, \tag{8}$$

where $\varepsilon = \left[\varepsilon_{11,}\varepsilon_{22,}\varepsilon_{33,}\gamma_{12,}\gamma_{23,}\gamma_{13}\right]^T$ represents the element strain, $\sigma = \left[\sigma_{11,}\sigma_{22,}\sigma_{33,}\sigma_{12,}\sigma_{23,}\sigma_{13}\right]^T$ represents the element stress, and S_d stands for the flexibility matrix after stiffness reduction. The expression is as follows:

$$S_d = \begin{bmatrix} \frac{1}{E_{11}(1-D_{11})} & -\frac{v_{12}}{E_{22}} & -\frac{v_{13}}{E_{33}} & 0 & 0 & 0 \\ -\frac{v_{12}}{E_{22}} & \frac{1}{E_{22}(1-D_{22})} & -\frac{v_{23}}{E_{22}} & 0 & 0 & 0 \\ -\frac{v_{13}}{E_{33}} & -\frac{v_{23}}{E_{22}} & \frac{1}{E_{33}(1-D_{33})} & 0 & 0 & 0 \\ 0 & 0 & 0 & \frac{1}{G_{12}(1-D_{44})} & 0 & 0 \\ 0 & 0 & 0 & 0 & \frac{1}{G_{23}(1-D_{55})} & 0 \\ 0 & 0 & 0 & 0 & 0 & \frac{1}{G_{13}(1-D_{66})} \end{bmatrix}, \tag{9}$$

where E_{11}, E_{22}, and E_{33} are the elastic moduli in three directions, G_{12}, G_{13}, and G_{23} are the shear moduli, v_{12}, v_{13}, and v_{23} are the Poisson's ratios, X_{1T} and Y_{2T} are the tensile strengths, and D_{11}, D_{22}, D_{33}, D_{44}, D_{55}, and D_{66} are damage variables, also known as stiffness reduction factors. They are used to quantify the degree of stiffness degradation of materials under different failure modes, with values typically in the range of [0,1]. The specific material parameters of the CFRP are shown in Table 1[15].

Table 1. Plain-weave CFRP material parameters (CFRP is the abbreviation for carbon fiber-reinforced polymer.)

E_{11}(GPa)	E_{22}(GPa)	E_{33}(GPa)	G_{12}(GPa)	G_{13}(GPa)	G_{23}(GPa)	v_{12}	v_{13}	v_{23}
68.68	68.68	8.5	11.66	4.5	4.5	0.13	0.41	0.41
X_{1T}(MPa)	X_{1C}(MPa)	Y_{2T}(MPa)	Y_{2C}(MPa)	Z_{3C}(MPa)	S_{12}(MPa)	S_{13}(MPa)	S_{23}(MPa)	
722.44	327.69	722.44	327.69	850	101.96	101.96	101.96	

The zero-thickness cohesive element employed a bilinear constitutive model, which was divided into two stages: damage initiation and damage evolution. When the traction force at the interface exceeded the interfacial strength, the cohesive element began to undergo damage. When the dissipated

energy during the element's damage process equaled the interfacial fracture toughness, it was judged that the element had completely failed, and delamination occurred between the layers. The Quads criterion [16] was used for damage initiation in the cohesive element:

$$\left(\frac{\sigma_{\mathrm{n}}}{N_{\max}}\right)^2+\left(\frac{\sigma_{\mathrm{s}}}{S_{\max}}\right)^2+\left(\frac{\sigma_{\mathrm{t}}}{T_{\max}}\right)^2=1, \tag{10}$$

$$\sigma_{\mathrm{n}}=E_{\mathrm{n}}\epsilon_{\mathrm{n}},\sigma_{\mathrm{s}}=E_{\mathrm{s}}\epsilon_{\mathrm{s}},\sigma_{\mathrm{t}}=E_{\mathrm{t}}\epsilon_{\mathrm{t}}, \tag{11}$$

where σ_{n}, σ_{s}, and σ_{t} represent the tensile stress in the out-of-plane direction 3 and the shear stresses in the in-plane directions 1 and 2 of the cohesive element, respectively, E_{n}, E_{s}, and E_{t} represent the elastic moduli in the three directions, respectively, ϵ_{n}, ϵ_{s}, and ϵ_{t} represent the strains in the three directions, respectively, and $N_{\max}$, $S_{\max}$, and $T_{\max}$ represent the tensile strength in the out-of-plane direction 3 and the shear strengths in the in-plane directions 1 and 2 of the cohesive element, respectively. When the Quads criterion equaled 1, it was determined that the element had been damaged and had entered the damage evolution stage.

The energy in this stage was primarily controlled through the following equation:

$$\left(\frac{G_{\mathrm{I}}}{G_{\mathrm{IC}}}\right)^2+\left(\frac{G_{\mathrm{II}}}{G_{\mathrm{IIC}}}\right)^2+\left(\frac{G_{\mathrm{III}}}{G_{\mathrm{IIIC}}}\right)^{\alpha}=1, \tag{12}$$

where G_{I}, G_{II}, and G_{III} represent the absorbed energies under the three failure modes of the cohesive element, G_{IC}, G_{IIC}, and G_{IIIC} represent the fracture toughnesses under the three failure modes of the cohesive element, G_{IC} represents the fracture toughness in the normal direction of the bonding plane, and G_{IIC} and G_{IIIC} represent the shear fracture toughnesses in two orthogonal directions within the interface. The exponent depends on the cohesive force. When the above formula was satisfied, the cohesive element had completely failed. Since the selected adhesive film bonding mechanical properties were similar to those of the interlaminar bonding mechanical properties of the CFRP, the material parameters of the cohesive element between the steel plate and CFRP layer, as well as between the CFRP layers, were consistent, as shown in Table 2 [16].

Table 2. Cohesive element material parameters

E_{n}(GPa)	E_{s}(GPa)	E_{t}(GPa)	$N_{\max}$(MPa)	$S_{\max}$(MPa)
8.5	3	3	60	60
$T_{\max}$(MPa)	G_{IC}(J·m^{-2})	G_{IIC}(J·m^{-2})	G_{IIIC}(J·m^{-2})	
60	0.4	1.6	1.6	

To simulate the temperature increase and the high strain rate state of the metal at the moment of the explosion, we used the *MAT_JOHNSON_COOK material constitutive model to describe the mechanical behavior of the Q235. The JOHNSON_COOK model was based on the von Mises yield stress model[17-19], with its state equation given by

$$\sigma=(A+B\varepsilon^n)\left[1+c\ln\left(\frac{\dot{\varepsilon}}{\dot{\varepsilon}_0}\right)\right][1-(T^*)^m], \tag{13}$$

where σ is the stress, A is the initial yield strength, B is the strain intensification index, n is the strain-hardening exponent, c denotes the strain-rate sensitivity coefficient, m is the thermal-softening exponent, ε is the plastic strain, $\dot{\varepsilon}$ is the strain rate, $\dot{\varepsilon_0}$ is the reference strain rate, $T^*=\frac{T-T_r}{T_m-T_r}$ is the dimensionless temperature, T is the actual temperature, T_m is the material melting point temperature, and T_r is the reference temperature.

The failure damage of the *MAT_JOHNSON_COOK model was mainly simulated using the cumulative damage failure model, and the damage degree of the unit in the failure model was calculated as follows:

$$D=\sum\frac{\Delta\bar{\varepsilon}^p}{\varepsilon^f}, \tag{14}$$

where the unit damage degree D was in the range of [0,1], $\Delta\bar{\varepsilon}^p$ is the time-step equivalent plastic strain increment, and ε^f is the current moment damage strain. $D = 0$ at the initial moment, and when D reached 1, material failure occurred. The expression for ε^f is as follows:

$$\varepsilon^f = [D_1 + D_2\exp(D_3\sigma^*)][1 + D_4 ln\dot{\varepsilon}^*][1 + D_5 T^*], \quad (15)$$

where σ^* is the stress triaxiality, and $D_1 - D_5$ are material constants. The material parameters and failure parameters are shown in Table 3.

Table 3. Q235 material parameters

A(MPa)	B(MPa)	C	m	n	D_1	D_2	D_3	D_4	D_5
229.0	439.0	0.1	0.55	0.503	0.3	0.9	-2.8	0	0

3.3 Model validation

Using the CONWEP algorithm built into ABAQUS to simulate explosive impact loads, Liu et al. [20] found that this algorithm exhibits high simulation accuracy and computational efficiency when calculating the dynamic responses of simple plates under explosive loads. The comparison between the finite element simulation results of the CONWEP algorithm for the CFRP–steel plate composite structure and the experimental structure is shown in Fig. 6. Delamination occurred between the carbon-fiber laminate and the steel plate. Based on the displacement curve, the final stable plastic deformation of the steel plate was 32.23 mm, with an error of 6.37% compared to the plastic displacement in the experiment. The exploded surface of the composite structure exhibited a cross-shaped crack, with lengths of 209 and 178 mm in the transverse and longitudinal directions, respectively, corresponding to errors of 6.63% and 7.23%, respectively, compared to the crack lengths in the experiment. The above results indicated that the plain-weave CFRP–steel plate finite element model had high accuracy.

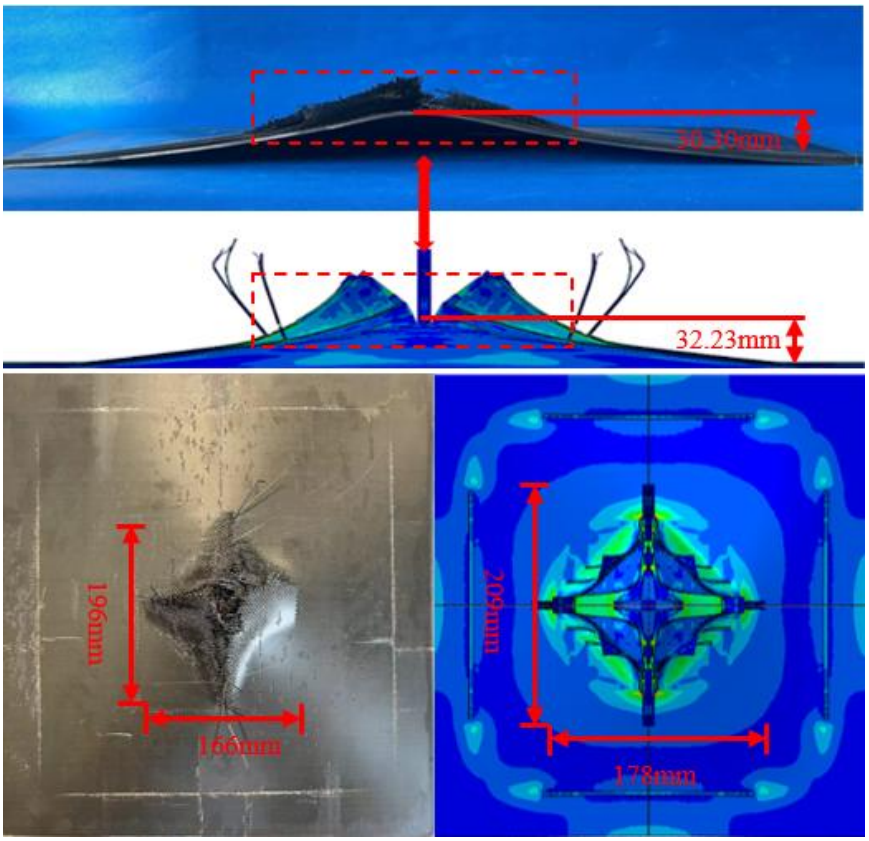


Figure. 6. Comparison of experimental and simulation damage results

4 Model establishment

4.1 Feature selection

4.1.1 Orthogonal experimental design

The orthogonal experimental design depicted in Fig. 7 is an efficient and rational experimental design method. Its objective is to eliminate interactions between different factors to the greatest extent possible by constructing an orthogonal array, thereby scientifically evaluating the impact of various levels of each factor on the response variable [21,22]. Given the high dimensionality of CFRP material parameters, orthogonal experiments can be employed to cover key parameter combinations under limited sample conditions, thus reducing the difficulty of data collection and decreasing the computational complexity of subsequent dimensionality reduction processing.

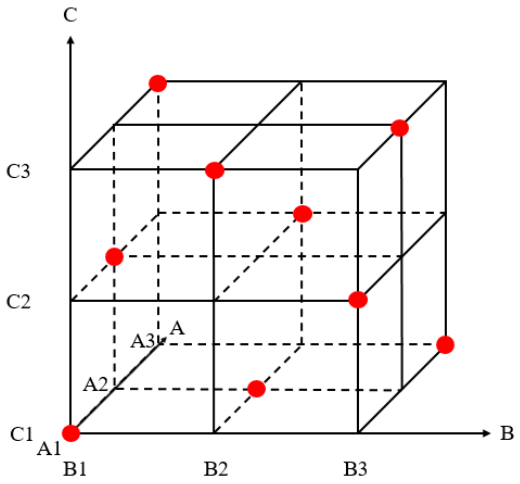


Figure. 7. Schematic diagram of orthogonal experimental design

Due to the 90° crossing and alternating arrangement of warp and weft fiber bundles in the plain woven CFRP, the mechanical properties in both directions were completely consistent, and thus, E_{11}=E_{22}, G_{13}=G_{23}, v_{13}=v_{23}, X_{1T}=Y_{2T}, X_{1C}=Y_{2C}, and S_{13}=S_{23}. There are 11 independent material parameters for CFRP, and the range of values for each parameter is divided into three levels. The level conditions of each parameter are shown in Table 4. An 11-factor, three-level orthogonal experimental design was conducted using the SPSS software, followed by simulation calculations. The plastic displacement and peak acceleration of the steel plates were taken as key indicators for evaluating the blast resistance. The specific calculation results are shown in Table 5 [23].

Table 4. Material parameter level

Constitutive parameter	Designation	Level 1	Level 2	Level 3
E_{11}/E_{22}(GPa)	X_1(GPa)	27	55.5	84
E_{33}(GPa)	X_2(GPa)	7	9	11
G_{12}(GPa)	X_3(GPa)	4.5	9.5	14
G_{13}/G_{23}(GPa)	X_4(GPa)	3.5	6.25	9
v_{12}	X_5	0.09	0.12	0.15
v_{13}/v_{23}	X_6	0.37	0.41	0.45
X_{1T}/Y_{2T}(MPa)	X_7(MPa)	425	677.5	930
X_{1C}/Y_{2C}(MPa)	X_8(MPa)	160	287.5	415
Z_{3C}(MPa)	X_9(MPa)	500	777.5	1055
S_{12}(MPa)	X_{10}(MPa)	63	96.5	130
S_{13}/S_{23}(MPa)	X_{11}(MPa)	55	69	83

Table 5. Results of orthogonal experimental design

ID	X_1	X_2	X_3	X_4	X_5	X_6	X_7	X_8	X_9	X_{10}	X_{11}	Plastic deformation (mm)	Peak acceleration (m/s^2)
1	1	1	1	3	2	3	3	3	3	2	1	33.47	3340650
2	1	3	3	2	2	3	1	3	2	3	3	31.16	4074980
3	1	2	2	1	2	3	2	3	1	1	2	25.92	2730740

4	1	1	1	2	3	2	2	2	2	3	1	37.83	2739340
5	1	1	1	1	1	1	1	1	1	1	1	37.22	2950160
…													
23	3	3	2	2	1	2	3	3	3	1	1	35.82	822649
24	3	1	3	1	3	3	3	1	2	2	2	33.68	3726770
25	3	3	2	3	3	3	1	1	1	3	1	43.10	3299100
26	3	1	3	3	1	2	2	3	1	3	2	33.35	2333980
27	3	2	1	1	1	2	1	3	2	2	3	38.19	2861850

4.1.2 Screening of key material parameters

Reddy et al. [24] pointed out that not all parameters in deep learning algorithms have a significant impact on model training. Ignoring the parameters with minor influences on the algorithm through dimensionality reduction techniques can alleviate the "curse of dimensionality" problem, thereby enhancing the training efficiency and prediction accuracy of the model. The random forest algorithm, as shown in Fig. 8, is a typical ensemble learning method that constructs multiple independent decision trees and makes predictions based on collective decision-making [25]. In the field of dimensionality reduction, the random forest algorithm achieves key parameter selection by calculating the importance of each feature, ultimately eliminating redundant features that contribute less to the model training. Utilizing the random forest algorithm for dimensionality reduction of the key material parameters of CFRP not only preserves the interpretability of the features, enabling the construction of subsequent prediction models, but also automatically captures the nonlinear relationships and high-order interaction responses between the material parameters and the structural protection performance, selecting the most important material parameters to better fit the data.

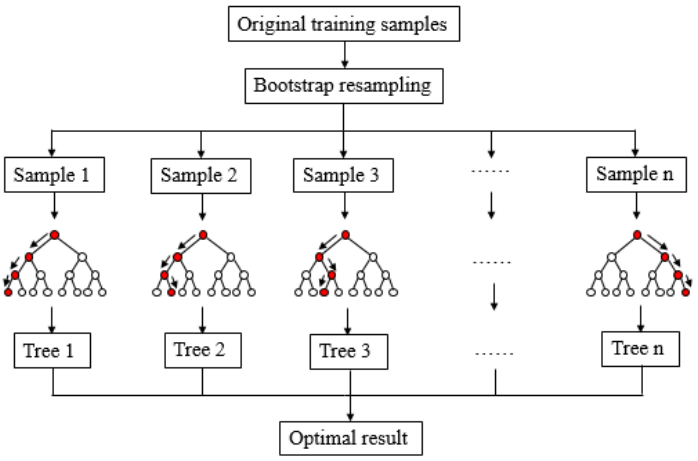
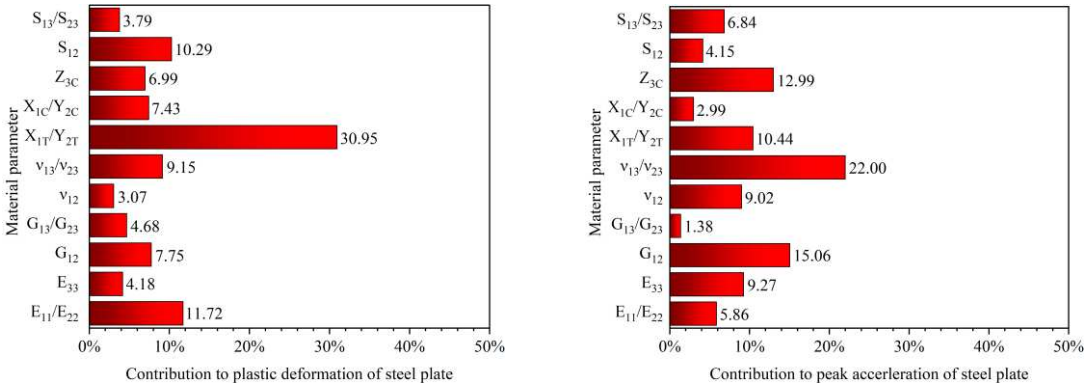


Figure. 8. Random forest algorithm

Two random forest regression models were trained separately for the plastic displacement and peak acceleration of the steel plate. Each model comprised 100 decision trees, and the random seed was fixed at 42 to ensure reproducibility. The feature importance values obtained for each response variable were normalized separately and subsequently combined using equal weights of 0.5 to obtain an overall importance score.

Figure 9 presents the feature importance of the CFRP material parameters for the two blast-response quantities, while Table 6 summarizes the individual feature-importance values, comprehensive importance scores, and corresponding rankings. According to the comprehensive ranking, the tensile strengths in the warp and weft directions X_{1T}/Y_{2T}, out-of-plane Poisson's ratios ν_{13}/ν_{23}, in-plane shear modulus G_{12}, and out-of-plane compressive strength Z_{3C} were identified as the four most influential material parameters. These parameters were therefore selected as the key input variables for the subsequent blast-response prediction models.



(a) Plastic deformation of steel plate (b) Peak acceleration of steel plate

Figure. 9. Contribution degree of CFRP material parameters

Table 6. Feature importance of CFRP material parameters for the blast responses of the composite structure

Parameters	Displacement Contribution	Acceleration Contribution	General Contribution
X_{1T}/Y_{2T}	30.95%	10.44%	20.695%
ν_{13}/ν_{23}	9.15%	22.00%	15.575%
G_{12}	7.75%	15.06%	11.405%
Z_{3C}	6.99%	12.99%	9.990%
E_{11}/E_{22}	11.72%	5.86%	8.790%
S_{12}	10.29%	4.15%	7.220%
E_{33}	4.18%	9.27%	6.725%
ν_{12}	3.07%	9.02%	6.045%
S_{13}/S_{23}	3.79%	6.84%	5.315%
X_{1C}/Y_{2C}	7.43%	2.99%	5.210%
G_{13}/G_{23}	4.68%	1.38%	3.030%

4.2 Data sampling

OLHS is an optimized and improved version of Latin hypercube sampling (LHS). It not only retains the advantage of projection uniformity in each dimension of the LHS method but also introduces optimization algorithms to ensure that the generated initial sample points maintain as uniform a distribution in the multidimensional space as possible [26,27]. A total of 50 sets of sample data were generated using the OLHS method, covering various values of the key material parameters of the CFRP, to evaluate the explosion-proof performance of plain woven CFRP–steel plate composite structures with different material parameters.

To visually display the distribution characteristics of the generated sample data, the sampling results were plotted on pair plots, as shown in Fig. 10. The histograms on the diagonal are the frequency distributions of individual material parameters, while the scatter plots of the upper and lower triangles show the relationships between any two parameters. From Fig. 10, it can be observed that the parameter values were uniformly distributed within the specified ranges, indicating that the sampling process achieved sufficient coverage of the parameter space.

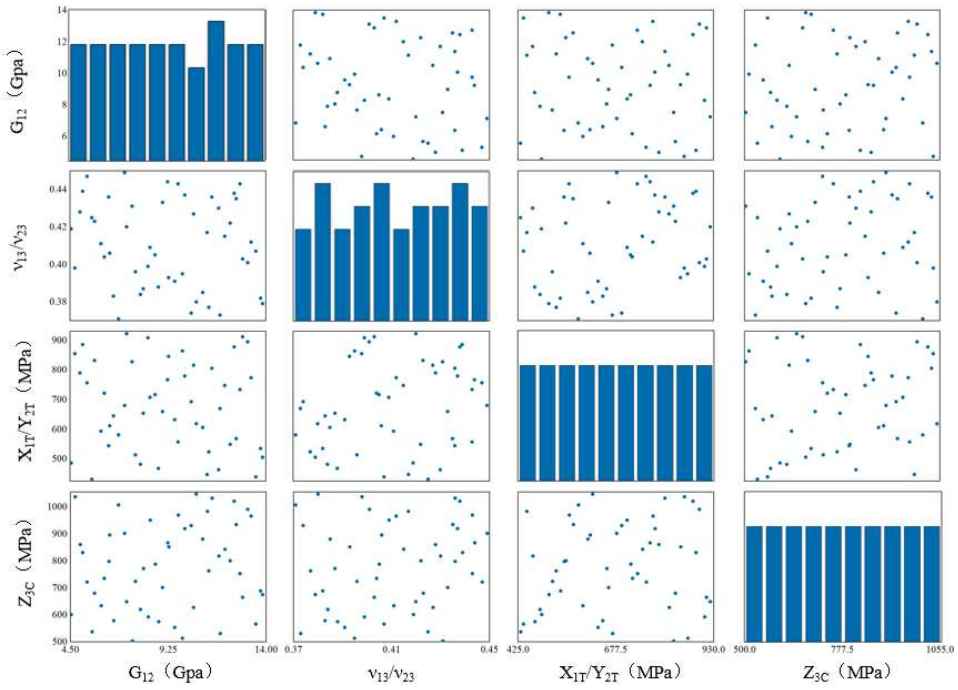


Figure. 10. Optimal Latin hypercube sampling results

By calculating the Pearson's correlation coefficient (PCC) for the different characteristic variables, the degree of linear correlation between them can be quantified [28]. The value range of the PCC is [−1, 1], and its absolute value indicates the strength of the linear correlation between two variables. When the PCC is close to −1 or 1, it indicates a strong positive or negative correlation between the two variables, whereas when the PCC is close to 0, it indicates no significant correlation between the two variables [29]. The PCC calculation results between different material parameters in the data generated by the aforementioned sampling are shown in Fig. 11. All the PCC values were less than 0.3, indicating a weak linear correlation between the key material parameters of the CFRP. This suggested that their impacts on the explosion-proof performance of the CFRP–steel plate composite structures were relatively independent.

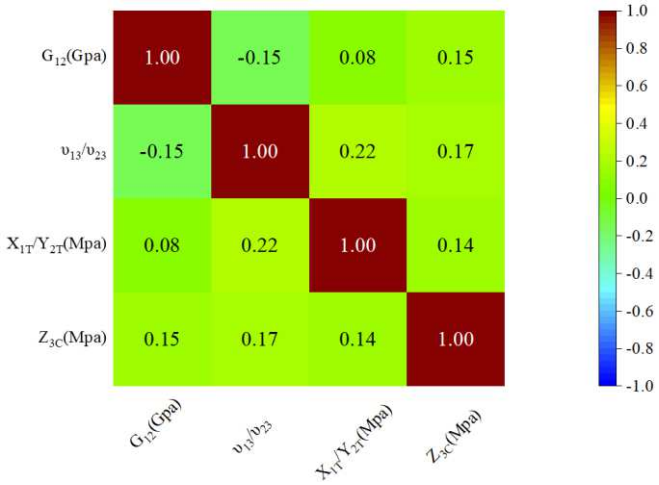
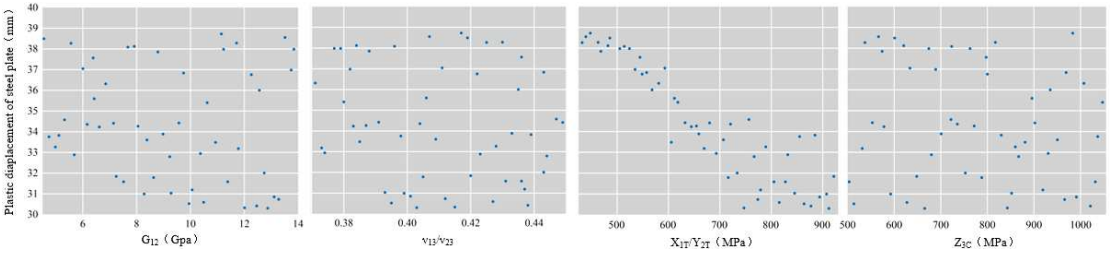


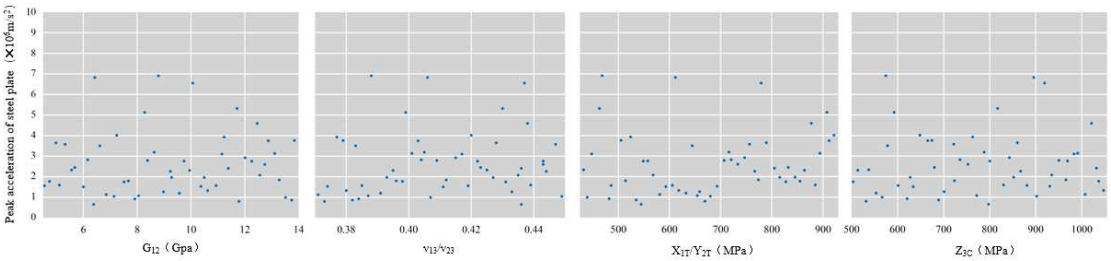
Figure. 11. Pearson's correlation coefficient heatmap

The blast resistance results corresponding to the data generated by sampling and obtained through finite element simulations are shown in Fig. 12. The influence of the CFRP material parameters on the blast resistance of the composite structures exhibited strong nonlinear characteristics, which were

difficult to effectively capture with traditional functions. Therefore, it was necessary to establish a mapping relationship between the material parameters and the structural protection performance through deep learning algorithms in order to construct a high-precision explosion-proof performance prediction model.



(a) Plastic deformation of steel plate



(b) Peak acceleration of steel plate

Figure. 12. Influence of material parameters on blast resistance

4.3 Model construction

4.3.1 Principles and methods

BPNN: This algorithm is a multi-layer feedforward neural network that calculates outputs through forward propagation and adjusts the model weights using backpropagation to minimize errors [30]. To prevent overfitting and enhance the model's generalization ability, regularization strategies such as L2 regularization or dropout are often employed [31].

RBF: This algorithm is a feedforward neural network that uses radial basis functions as the activation function in the hidden layer. The center and width parameters of the hidden layer are determined through unsupervised learning, while the weights of the output layer are optimized through supervised learning, achieving nonlinear mapping from input to output [32].

GRNN: This algorithm is a feedforward neural network based on radial basis functions, consisting of an input layer, a pattern layer, a summation layer, and an output layer. The pattern layer calculates the similarity between the input sample and the training samples, while the summation layer calculates the weighted sum of the outputs and the simple sum of the outputs separately and finally obtains the output result through the ratio [33].

EHO-GRNN: The core of this algorithm lies in utilizing the global search capability of the elephant herding optimization (EHO) algorithm to address the dependency of the GRNN on key parameters. In the EHO-GRNN algorithm, the kernel function smoothing factor of the GRNN is treated as an individual in the elephant herd, with the prediction error serving as the fitness function to evaluate the quality of the individuals. Continuous velocity and position updates are performed to find the optimal smoothing factor value that maximizes the prediction performance of the GRNN. Simultaneously, clan recombination is carried out every certain number of iterations to enhance the population diversity, ultimately yielding a GRNN model with the optimal prediction performance.

IEHO-GRNN: This algorithm improves the EHO-GRNN algorithm through the following

equations:

$$F = \frac{1}{n}\sum_{i=1}^{n} \log\left[1 + m \times \left(y_{i,\text{norm}} - \hat{y}_{i,\text{norm}}\right)^2\right] + \frac{k}{K}|\lambda_k - \lambda_{k-1,\text{best}}|, \tag{16}$$

$$c_1 = c_{1\min} + (c_{1\max} - c_{1\min}) \times \frac{k}{K} \times e^{-\frac{\sigma_F}{F}}, \tag{17}$$

$$c_2 = c_{2\max} - (c_{2\max} - c_{2\min}) \times \frac{k}{K} \times e^{-\frac{\sigma_F}{F}}, \tag{18}$$

where F represents the fitness value of different individuals in the population, n denotes the number of samples in the training set, m stands for the amplification factor, typically set to 100, $y_{i,\text{norm}}$ signifies the normalized true value of the ith training sample, and $\hat{y}_{i,\text{norm}}$ represents the normalized predicted value of the ith training sample. k is the current iteration count, K represents the maximum iteration count, λ_k is the smoothing factor at the kth iteration, $\lambda_{k-1,\text{best}}$ denotes the optimal smoothing factor in the population at the (k−1)th iteration, c_1 and c_2 are the individual learning factor and social learning factor, respectively, c_{1min} and c_{2min} are the minimum values of the individual learning factor and social learning factor, respectively, typically set to 1.5, $c_{1\max}$ and $c_{2\max}$ are the maximum values of the individual learning factor and social learning factor, respectively, typically set to 2.5, σ_F signifies the standard deviation of the fitness values of different individuals in the population, and $\bar{F}$ represents the mean fitness of the different individuals in the population.

4.3.2 Hyperparameter tuning of model

In deep learning, the prediction models of different neural networks all rely on a set of hyperparameters, which have a significant impact on the model's prediction accuracy, convergence speed, and generalization ability. Unlike model parameters that are automatically learned through the training process, hyperparameters (such as the number of hidden layers, number of neurons, learning rate, batch size, and iteration count) need to be manually set before model training [34]. Hyperparameter tuning aims to find the optimal combination of parameters to enhance the overall performance of the model [35]. A random search is a commonly used hyperparameter optimization method, which involves randomly sampling combinations of hyperparameters within a preset range and then selecting the combination that minimizes the loss function based on the model training results. The optimized hyperparameter configurations for different deep learning models are shown in Table 7.

Table 7. Optimal hyperparameters for different deep learning methods

Model	Hyperparameter	Range	Optimal values for different performances	
			Plastic deformation of steel plate	Peak acceleration of steel plate
BPNN	Number of hidden layers	1-5	4	4
	Neurons for hidden layers	2-32	(12,15,12,18)	(5,18,3,7)
	Activation function	sigmoid,tanh,relu	relu	relu
	Optimizer	lbfgs,sgd,adam	adam	adam
	Maximum number of iterations	100-10000	8210	6496
	L2 penalty factor	0.0001-0.1	0.0638	0.0002
	Batch size	8-50	34	28
	Learning rate	0.0001-0.1	0.0473	0.0305
RBF	Radial basis function	gaussian,polynomial, laplacian	gaussian	gaussian
	Neurons for hidden layers	2-32	17	20
	Gaussian kernel width	0.1-10	3.3208	9.0776
	Center point selection	clustering,random selection	clustering	clustering

	L2 penalty factor	0.0001-0.1	0.0046	0.0357
	Gaussian kernel width	0.1-10	0.3083	9.9712
GRNN	Kernel function	gaussian,polynomial, laplacian	gaussian	gaussian
	Center point selection	clustering,random selection	clustering	clustering
	Maximum number of iterations	100-10000	8204	9803
EHO-GRNN	Population size	10-1000	681	856
	Number of clans	10-1000	227	107
	Initial inertia weight	0.8-1.0	0.98	0.99
	Learning factor	1.5-2.5	2.38,2.01	2.08,1.93
	Maximum number of iterations	100-10000	981	5651
IEHO-GRNN	Population size	10-1000	232	780
	Number of clans	10-1000	29	15
	Initial inertia weight	0.8-1.0	0.96	0.96

The 5-fold cross-validation method shown in Fig. 13 is commonly used to evaluate the dependence of different neural network models on the data after tuning. This method divides the training data into five mutually exclusive subsets, where the first fold (Fold1) is used as the test set for error estimation, and the remaining folds are used as the training set for model training. The validation is repeated five times in turn [36]. Finally, the prediction errors of the five validation results are averaged to obtain the evaluation metric of the model, which reflects the model's generalization ability.

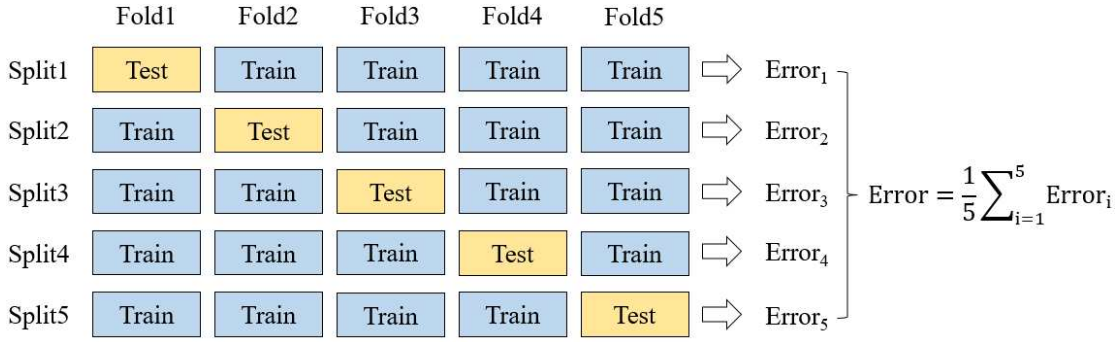


Figure. 13. Diagram of 5-fold cross-validation process

The prediction models for the blast resistance of the CFRP–steel plate composite structures were evaluated using mean squared error (MSE), mean absolute error (MAE), root mean square error (RMSE), mean absolute percentage error (MAPE), and coefficient of determination (R^2). These indicators were used to assess the degree of deviation between the actual and predicted values. The specific calculations are shown as follows:

$$MSE = \frac{1}{n}\sum_{i=1}^{n}(y_i - \hat{y}_i)^2, \tag{19}$$

$$MAE = \frac{1}{n}\sum_{i=1}^{n}|y_i - \hat{y}_i|, \tag{20}$$

$$RMSE = \sqrt{\frac{1}{n}\sum_{i=1}^{n}(y_i - \hat{y}_i)^2}, \tag{21}$$

$$MAPE = \frac{1}{n}\sum_{i=1}^{n}\left|\frac{y_i - \hat{y}_i}{y_i}\right| \times 100\%, \tag{22}$$

$$R^2 = 1 - \frac{\sum_{i=1}^{n}(y_i - \hat{y}_i)^2}{\sum_{i=1}^{n}(y_i - \bar{y})^2}, \tag{23}$$

where n represents the sample size, y_i denotes the actual value of the blast resistance metric for the i_{th} sample, $\hat{y}_i$ signifies the predicted value of the blast resistance metric for the i_{th} sample, and $\bar{y}$ stands for the average of the actual values of the blast resistance metric.

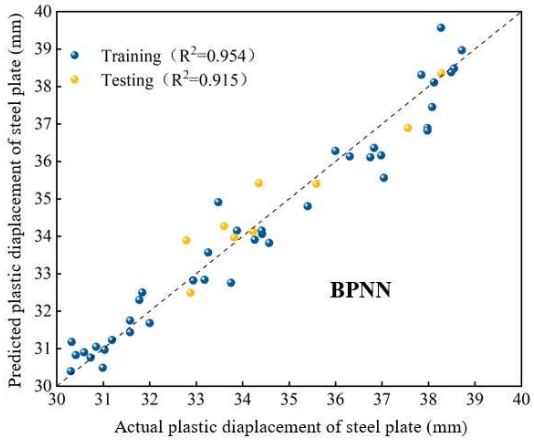
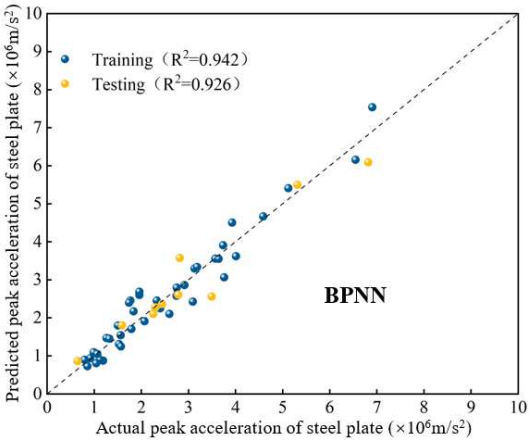
5 Results and discussion

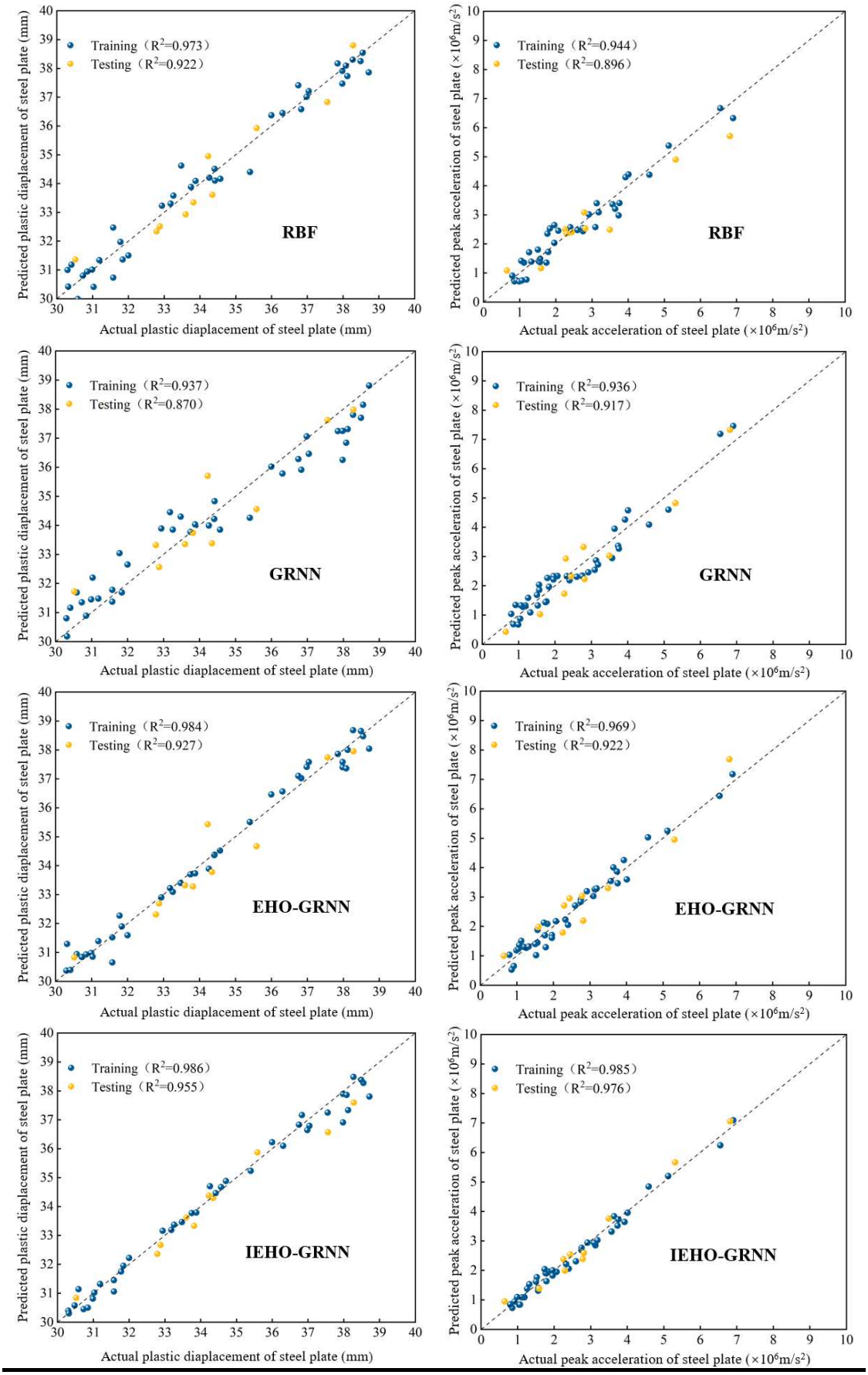
5.1 Evaluation of model prediction accuracy

The neural network models, after hyperparameter tuning, were used to predict the blast resistance of CFRP–steel plate composite structures. The comparison between the actual and predicted values is shown in Table 8. R^2 was used to quantify the correlation between the predicted and actual values of the blast resistance, with a higher value indicating a higher fitting accuracy of the neural network model [37]. When using the IEHO-GRNN algorithm for prediction, the R^2 values for the training and test datasets for the steel-plate plastic displacement were 0.986 and 0.955, respectively, while those for the training and test datasets for the steel-plate peak acceleration were 0.985 and 0.976, respectively. In the scatter plots of the IEHO-GRNN algorithm, the points were more concentrated near the centerline than they were for the scatter plots of the other models, indicating that its model fitting performance was the best.

The high accuracy of the IEHO-GRNN algorithm can be attributed to the fitness function and learning factor shown in Eqs. (1)–(3). For the fitness function, the first term could more sensitively reflect the performance differences between different individuals in the population, facilitating the algorithm to select better individuals and avoiding the excessive influence of large errors on the fitness value, which helped the algorithm maintain stability during the search process. The second term allowed the algorithm to search for parameters over a wide range in the early stages of iteration, enhancing the global search capability, and forced the parameters to converge near the historical optimal solution in the later stages of iteration, strengthening the local search capability. The learning factor could limit the search range to the vicinity of the current individual when the diversity of the population was low, reducing the number of unnecessary searches, improving the search efficiency, and saving computational resources. When the diversity of the population was high, it continuously tried new areas in the entire space, reducing the risk of falling into local optima.

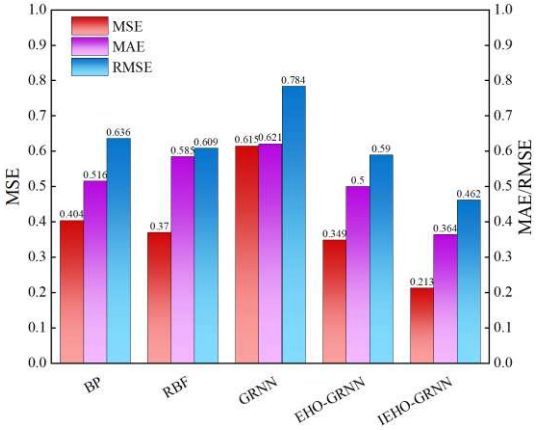
Table 8. Comparison between actual and predicted blast resistance values

Plastic deformation of steel plate	Peak acceleration of steel plate
	

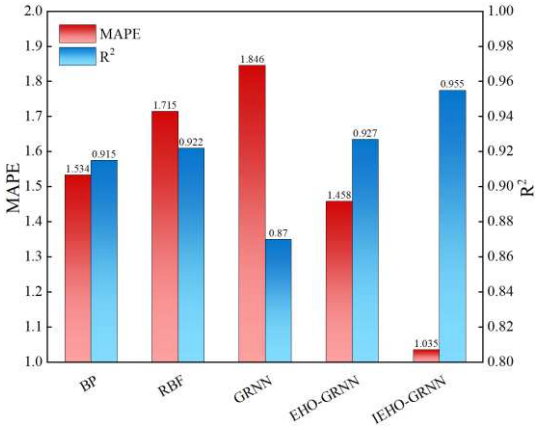


The predictive performance metrics (MSE, MAE, RMSE, MAPE, and R^2) of the different deep learning algorithms for the blast resistance of the CFRP–steel plate composite structures are shown in

Figs. 14 and 15. For the plastic displacement of the steel plate, the IEHO-GRNN algorithm yielded the highest R^2 value of 0.955, with the lowest MSE, MAE, RMSE, and MAPE values of 0.213, 0.364, 0.462, and 1.035%, respectively. For the peak acceleration of the steel plate, the IEHO-GRNN algorithm yielded the highest R^2 value of 0.976, with the lowest MSE, MAE, RMSE, and MAPE values of 0.706×10^{11}, 2.502×10^{5}, 2.658×10^{5}, and 12.194%, respectively. Therefore, compared to other deep learning models, the IEHO-GRNN algorithm exhibited more accurate prediction precision for the blast resistance of the CFRP–steel plate composite structures.

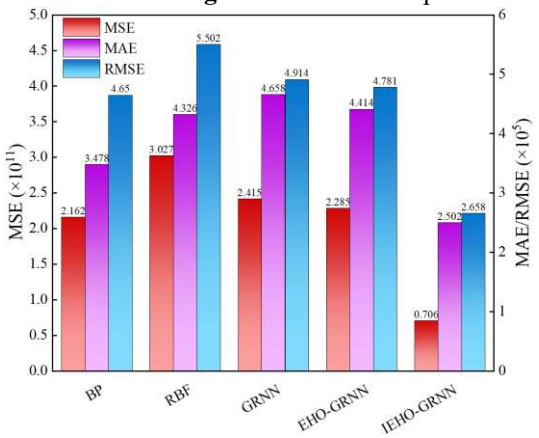


(a) MSE, MAE, and RMSE values

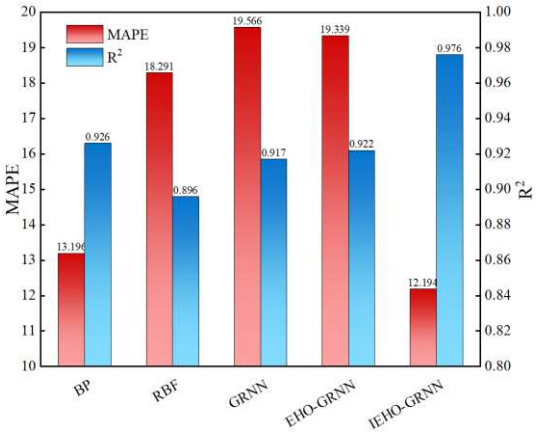


(b) MAPE and R^2 values

Figure. 14. Predictive performance for steel-plate plastic displacement



(a) MSE, MAE, and RMSE values



(b) MAPE and R^2 values

Figure. 15. Predictive performance for steel-plate peak acceleration

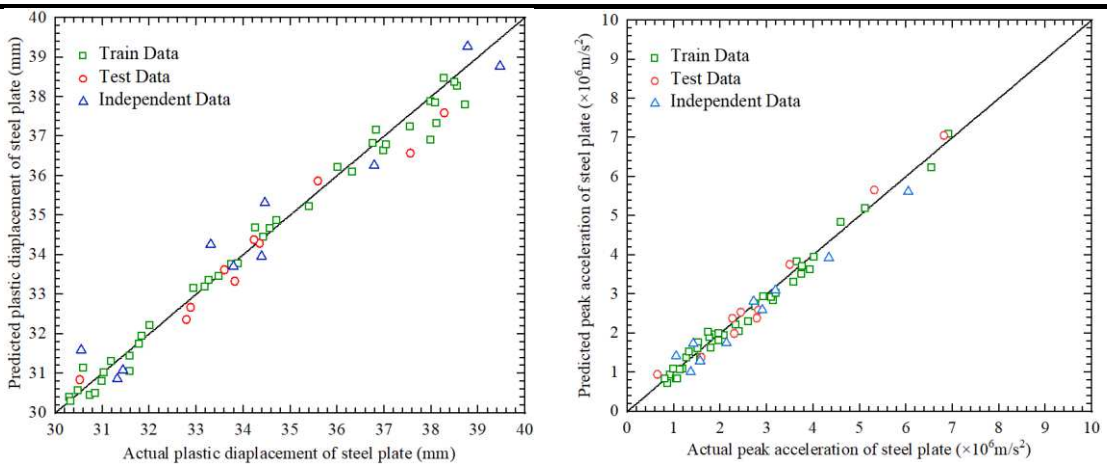
5.2 hold-out FE simulation set validation analysis

To evaluate the generalization ability of the IEHO-GRNN algorithm on different datasets, an hold-out FE simulation set was required to validate the model [38]. In addition to the original 50 datasets, an additional 10 datasets were generated as hold-out FE simulation sets through OLHS. The hold-out FE simulation set were only used for model validation, not for training and testing. After completing the hyperparameter tuning, the validation results of the IEHO-GRNN algorithm on the hold-out FE simulation set are shown in Table 8. From the results in Tables 8 and 9, it can be seen that for the plastic displacement of the steel plates, the R^2 values of the IEHO-GRNN model on the training set, test set, and hold-out FE simulation set were 0.986, 0.955, and 0.950, respectively, indicating that the differences in the R^2 values of the test set and hold-out FE simulation set from that of the training set were 3.14% and 3.65%, respectively. For the peak acceleration of the steel plate, the R^2 values of the model on the training set, test set, and hold-out FE simulation set were 0.985, 0.976, and 0.952, respectively, indicating that the differences in the R^2 values of the test set and hold-out FE simulation set from that of the training set were 0.91% and 3.35%, respectively. The above results indicated that

the IEHO-GRNN algorithm was not sensitive to the prediction results on the hold-out FE simulation set, meaning that this algorithm can be used for predicting the blast resistance of CFRP–steel plate composite structures. The prediction results of the IEHO-GRNN algorithm on the training set, test set, and hold-out FE simulation set are shown in Fig. 16, further verifying its prediction consistency on the hold-out FE simulation set.

Table 9. Model validation analysis

ID	G_{12} (GPa)	v_{13}/v_{23}	X_{1T}/Y_{2T} (MPa)	Z_{3C} (MPa)	Plastic deformation of steel plate		Peak acceleration of steel plate	
					Actual value (mm)	Predictive value (mm)	Actual value (m/s^2)	Predictive value (m/s^2)
1	13.26	0.43	634.14	516.80	33.31	34.26	2904910	2591131
2	8.21	0.39	689.56	567.37	33.79	33.71	1565130	1290436
3	5.33	0.41	557.77	948.06	36.79	36.26	1049310	1414342
4	6.74	0.39	453.11	820.39	39.47	38.77	4339630	3928698
5	12.52	0.44	736.70	631.44	30.55	31.59	3184310	3091836
6	10.43	0.45	830.48	672.43	31.44	31.08	2132910	1747403
7	9.46	0.38	906.43	775.07	31.32	30.86	6047320	5616444
8	11.95	0.37	488.39	1001.30	38.78	39.27	1363830	1007307
9	8.94	0.42	603.29	933.48	34.46	35.51	2717960	2816163
10	6.28	0.41	817.54	851.33	34.39	33.96	1418880	1734094
R^2					0.950		0.952	



(a) Plastic displacement dataset results (b) Peak acceleration dataset results

Figure. 16. Training, test, and hold-out FE simulation set results of the IEHO-GRNN algorithm

6 Conclusion

Firstly, this paper verified the accuracy of the explosion simulation model for CFRP-reinforced steel plate composite structures through near-field air explosion test. Based on this, the IEHO-GRNN algorithm was proposed, and a prediction model for structural protection performance was constructed. The main conclusions are as follows:

(1) The explosion numerical simulations of the CFRP–steel plate composite structure had high accuracy. The simulation result of the final plastic deformation of the steel plate had an error of 6.37% compared to the experiment. The errors of the length of the crack on the exposed surface of the composite structure in the horizontal and vertical directions were 6.63% and 7.23%, respectively. This model can be used to perform dimensionality reduction of the material parameters and predict the data points required for model training.

(2) By combining orthogonal experiments and the random forest algorithm, G_{12}, v_{13}/v_{23}, X_{1T}/Y_{2T}, and Z_{3C} were identified as key material parameters affecting the structural protective performance. Based on 50 sets of data generated using OLHS and PCC analysis, The OLHS samples exhibited low pairwise linear correlations, indicating satisfactory statistical space-filling characteristics of the

sampling design.

(3) A predictive model for the protective performance of CFRP-reinforced steel-plate composite structures was established based on five algorithms: BPNN, RBF, GRNN, EHO-GRNN, and IEHO-GRNN. The comprehensive evaluation of five error metrics, namely MSE, MAE, RMSE, MAPE, and R^2, indicated that the IEHO-GRNN algorithm exhibited the highest prediction accuracy.

(4) A sensitivity analysis was conducted on the prediction model established by the IEHO-GRNN algorithm using an hold-out FE simulation set. It was found that the differences in the R^2 values of the test set and the hold-out FE simulation set from that of the training set were 3.14% and 3.65%, respectively, in the prediction of steel-plate plastic displacement, and 0.91% and 3.35%, respectively, in the prediction of steel-plate peak acceleration. This indicated that the algorithm has satisfactory performance within the investigated domain.

This study addressed the issues that deep learning algorithms are currently facing, such as the tendency to become trapped in local optima, low search efficiencies, and poor generalization abilities. The IEHO-GRNN algorithm was proposed, which not only predicts the structural protection performance based on the key material parameters of CFRP but also provides researchers with a more scientific method for optimizing the CFRP performance. However, The applicability of the proposed surrogate is restricted to the prescribed plate configuration, boundary condition, material-parameter domain, and 200 g TNT-equivalent CONWEP loading condition. Its extrapolation to other charge masses, stand-off distances, and structural configurations requires additional validation.

CRediT authorship contribution statement

Xiaowang Sun: Conceptualization, Data curation, Funding acquisition. Hao Sun: Formal analysis Validation, Writing – original draft . Jiahao He: Investigation ,Methodology. Hejing Hou: Software, Visualization. Haopeng Bao: Supervision. Xianhui Wang: Investigation, Resources. Tao Wang: Visualization, Writing–review & editing. Tiaoqi Fu: Project administration. Sha Chen: Software, Visualization. Tingjun Liu: Visualization.

Declaration of Competing Interest

No conflict of interest exists in the submission of this manuscript, and manuscript is approved by all authors for publication.

Acknowledgments

The authors would like to thank the funding Supported by the National Natural Science Foundation of China (Grant No. 52272370)References.

[1] P.A. Shirbhate, M.D. Goel, A critical review of blast wave parameters and approaches for blast load mitigation, Archives of Computational Methods in Engineering. 28 (2021) 1713-1730.

[2] Z.D. Liu, X.H. Zhao, H.Y. Fang, G.H. Wang, M.S. Shi, Investigation on the damage features and dynamic response of reinforced concrete slabs with polyurethane sacrificial cladding under close-range explosions, Construction and Building Materials. 395 (2023) 132149.

[3] Heriana, F.E.H. Jatmiko, F. Muhammad, B.K. Hadi, L. Guanwan, Guanryo, Experimental investigation of the performances of thick CFRP, GFRP, and KFRP composite plates under ballistic impact, Science and Engineering of Composite Materials. 31(2024) 20220240.

[4] J.J. Kim, Design Optimization of explosion-resistant system consisting of steel slab and CFRP frame, Materials. 14 (2021) 2589.

[5] A. Sayam, A.N.M.M. Rahman, M.S. Rahman, S.A. Smriti, F. Ahmed, M.F. Rabbi, M. Hossain, M.O. Faruque, A review on carbon fiber-reinforced hierarchical composites: mechanical performance, manufacturing process, structural applications and allied challenges, Carbon

Letters. 32 (2022) 1173-1205.

[6] S.H. Gao, W.X. Zhang, K.F. Yang, X.Y. Wang, Z.P. Feng, Comparison of different prediction methods for heat transfer distribution of lantern-shaped pin-fin channel with different deep learning surrogate models, Journal of Xi'an Jiaotong University. 58 (2024) 31-42. (In China)

[7] J.J. Zhang, D. Wang, Static strength reliability and sensitivity analysis of large composite structures based on surrogate models, Acta Materiae Compositae Sinica. 42 (2025) 570-578. (In China)

[8] A. Ammar, A. Amna, D. Vassilis, D. Haris, B. Imad, M. Maher, Predicting mechanical properties of CFRP composites using data-driven models with comparative analysis, Plos one. 20 (2025) 0319787.

[9] J.J Cao, B. Niu, M.J Zhang, Study on the prediction model of bullet proof performance of glass fiber reinforced composites based on improved neural network, Journal of Ordnance Equipment Engineering. 44 (2023) 163-169. (In China)

[10] M.S. Li, W. Wu, B.S. Chen, L.X. Guan, Y. Wu, Prediction of properties of starch matrix foam composites by radial basis function artificial neural network based on improved particle swarm optimization, Acta Materiae Compositae Sinica. 34 (2017) 2882-2889. (In China)

[11] A. Saravanakumar, L. Rajeshkumar, D. Balaji, M.P.J. Karunan, Prediction of wear characteristics of AA2219-Gr matrix composites using GRNN and Taguchi-based approach, Arabian Journal for Science and Engineering. 45 (2020) 9549-9557.

[12] D.P Xu, X.W Sun, Y. Liu, X.S. Zhang, X.H. Wang, J.H. He, K. Wu, T.Q. Fu, J. Tang, Anti-explosion performance of plain woven CFRP-steel composite structure, Acta Materiae Compositae Sinica. 42 (2025) 6635-6649. (In China)

[13] M. Gupta, H. Singh, A.N. Khan, P. Mahajan, R.T.D. Prabhakaran, R. Alagirusamy, An improved orthotropic elasto-plastic damage model for plain woven composites, Thin-Walled Structures. 162 (2021) 107598.

[14] G.G. Sha, W. Xiao, X.H. Lu, H.F. Zuo, M.S. Cao, W. Ostachowicz, Enhancing compressive failure prediction in repaired composites: A comparative study of 2D and 3D Hashin criteria with experimental validation, Thin-Walled Structures. 217 (2025) 113911.

[15] X.S. Zhang, X.W. Sun, X.H. Wang, T.Z. Yao, S.Y. Xiao, D.P. Xu, T.Q. Fu, J.H. He, Effects of stress state and strain rate on the in-plane mechanical behavior of plain woven CFRP, Acta Materiae Compositae Sinica. 42 (2025) 3535-3547. (In China)

[16] B. Alanbay, R.C. Batra, Optimization of blast mitigating sandwich structures with fiber-reinforced face sheets and PVC foam layers as core, Thin-Walled Structures. 179 (2022) 109721.

[17] V.K.R. Sirigiri, V.Y. Gudiga, U.S. Gattu, G. Suneesh, K.M. Buddaraju, A review on Johnson Cook material model, Materials Today: Proceedings. 62 (2022) 3450-3456.

[18] L. Wang, J.H. Kong, D.Y. Chu, Y.F. Wang, T. Wang, Z.L. Liu, Enhancing ballistic performance: Effect of polyurea coating on backface deformation of UHMWPE laminates, Composite Structures. 355 (2025) 118846.

[19] J.H. He, W.W. Qin, T.Z. Yao, J. Tang, X.W. Sun, D.W. Pi, X.H. Wang, X.M. Wen, Blast resistance and protection mechanism of glass fiber mesh reinforced polyurea (PU-GFM)/steel plate composite structures. Construction and Building Materials, 2025, 472:140879.

[20] T. Liu, C.H. Chen, H. Li, Y.W. Yu, Y.S. Cheng, An efficient and accurate numerical method for simulating close-range blast loads of cylindrical charges based on neural network, Defence Technology. 44 (2025) 257-271.

[21] J.M. Liu, X.Z. Wang, H. Cheng, H.X. Fan, Orthogonal design and microstructure mechanism analysis of novel bentonite polymer slurry in pipe jacking, Polymers. 15 (2023) 1461.

[22] M. Anxhelina, A.B. Thomas, Q. Elsa, A. Ramadan, Z. Milazim, Multi-response optimization on hydrated calcium aluminate rich ternary binders using taguchi design of experiments and principal component analysis, Buildings. 13(2023) 2494.

[23] H.R. Cui, J.H. Huang, Y. Yan, A Sentiment-driven SPSS requirement analysis method based on online reviews, Procedia CIRP. 128 (2024) 834-839.

[24] G.T. Reddy, M.P.K. Reddy, K. Lakshmanna, R. Kaluri, D.S. Rajput, G. Srivastava, Analysis of dimensionality reduction techniques on big data, IEEE Access. 8 (2020) 54776-54788.

[25] Y. Lin, X.L. Zhu, Z.G. Zheng, Z. Dou, R.L. Zhou, The individual identification method of wireless device based on dimensionality reduction and machine learning, The Journal of Supercomputing. 75 (2019) 3010-3027.

[26] M. Zhu, B. Wang, T.T. Liu, J.W. Yao, X. Chen, C.S. Zhou, W.X. Li, An enhanced intelligent-driven learning framework for adaptive multi-objective optimization control of pintle solid-fuel rocket engines, Energy. 347 (2026) 140405.

[27] C.M. Sun, H.H. Lin, Y.Y. Wu, Y.F. Duan, CFD-neural network collaborative optimization drives aerodynamic drag reduction of container ship fairings, Ocean Engineering. 342 (2025) 122971.

[28] E.H.D. Heuvel, Z.Z. Zhan. Myths about linear and monotonic associations: Pearson's r, Spearman's ρ, and Kendall's τ, The American Statistician. 76 (2022) 44-52.

[29] Z.Q. Zeng, W.Y. Liang, T.L. Wang, Z.Y. Hong, Q.L. Chang, S.L. Yang, A method for predicting the capacity of lithium-ion batteries based on Pearson correlation coefficient-guided multi-objective particle swarm optimization, Computers & Industrial Engineering. 210 (2025) 111514.

[30] K.J. Xue, J.S. Wang, Y. Chen, H. Wang, Improved BP neural network algorithm for predicting structural parameters of mirrors, Electronics. 13 (2024) 2789.

[31] R.Y. Li, Q. Deng, D. Tian, D.Y. Zhu, B. Lin, Predicting perovskite performance with multiple machine-learning algorithms, Crystals. 11 (2021) 818.

[32] F. Wurzberger, F. Schwenker, Learning in deep radial basis function networks, Entropy. 26 (2024) 368.

[33] H.K. Ghritlahre, R.K. Prasad, Exergetic performance prediction of solar air heater using MLP, GRNN and RBF models of artificial neural network technique, Journal of Environmental Management. 223 (2018) 566-575.

[34] S. Roy, R. Mehera, R.K. Pal, S.K. Bandyopadhyay, Hyperparameter optimization for deep neural network models: a comprehensive study on methods and techniques, Innovations in Systems and Software Engineering. 21 (2023) 789-800.

[35] F. Kuran, G. Tanırcan, E. Pashaei, Performance evaluation of machine learning techniques in predicting cumulative absolute velocity, Soil Dynamics and Earthquake Engineering. 174 (2023) 108175.

[36] D. Wilimitis, C.G. Walsh, Practical considerations and applied examples of cross-validation for model development and evaluation in health care: Tutorial, JMIR AI. 2 (2023) 49023.

[37] P.W. Guo, W.N. Meng, M.F. Xu, V.C. Li, Y. Bao, Predicting mechanical properties of high-performance fiber-reinforced cementitious composites by integrating micromechanics and machine learning, Materials. 14 (2021) 3143.

[38] D.K. Bhamare, P. Saikia, M.K. Rathod, D. Rakshit, J. Banerjee, A machine learning and deep learning based approach to predict the thermal performance of phase change material integrated

building envelope, Building and Environment. 199 (2021) 107927.